scientific reports

OPEN

Intense multicycle THz pulse generation from laser-produced nanoplasmas

Manoj Kumar[1], Hyung Seon Song[1], Jaeho Lee[1], Dohyun Park[1], Hyyong Suk[2] & Min Sup Hur[1]✉

We present a novel scheme to obtain robust, narrowband, and tunable THz emission using a nano-dimensional overdense plasma target, irradiated by two counter-propagating detuned laser pulses. So far, no narrowband THz sources with a field strength of GV/m-level have been reported from laser-solid interaction (mostly half-or single-cycle THz pulses with only broadband frequency spectrum). From two- and three-dimensional particle-in-cell simulations, we find that the strong plasma current generated by the beat ponderomotive force in the colliding region, produces beat-frequency radiation in the THz range. Here we report intense THz pulses ($f \simeq 30$THz) with an unprecedentedly high peak field strength of 11.9 GV/m and spectral width ($\Delta f / f \simeq 5.3\%$), which leads to a regime of an extremely bright narrowband THz source of TW/cm^2, suitable for various ambitious applications.

In recent years, terahertz (THz) radiation sources have identified potential in a variety of research and industrial fields including biomedical imaging, time-resolved molecular spectroscopy, communication, and security[1–9]. Despite the rapid advances in THz science today, developing intense and compact THz radiation sources remains challenging. Great strides have been made in crystal-based THz devices[10–15] that generate sub-millijoule energies of THz pulses with conversion efficiencies reaching around 1%. However, it is difficult to scale up to higher energies since the crystals can be damaged at high intensities of driving laser pulses. By contrast, plasma can overcome the problem of optical damage to crystals, because it can sustain extremely high-amplitude electromagnetic oscillations. Such characteristics of plasmas have attracted considerable attention as intense and powerful THz sources[16–20]. Mechanism-wise, ionization current in laser-induced plasma[21–25], coherent transition radiation (CTR)[26–31], sheath radiation (SR) associated with energetic ions[32,33], and experimentally laser-solid target interactions[34–39] generated up to GV/m electric field with 0.1% conversion efficiency. Recently, structured targets were used to enhance the THz emission by increased laser absorption[40–42].

The systems described above generate very intense and high-power, but mostly half- or single-cycle THz pulses, which have a broad frequency spectrum. The broadband pulses are useful for ultrafast pump-probe experiments where the THz pulse can be used as a strong DC electric bias field or spectroscopic study of materials[43]. However, spectral density at a particular, desired frequency is inevitably low, hence they are not suitable for applications that require monochromatic THz waves, e.g. THz-driven accelerator[44] or pump-probe experiments for molecular bonding[45–47]. For plasma-based narrowband THz sources, plasma oscillation[17,19] can be used as a radiating antenna, but low coupling efficiency between plasma wave and THz radiation matters. Another method is generating THz emission at the beating frequency of two laser pulses that co-propagate through underdense plasmas[20]. In this case, conversion of beat-to-THz is technically difficult and inefficient, and most of all, the plasma current that is responsible for THz emission is weak in underdense plasmas. Other than those ideas, the free-electron laser is only a narrowband source in a high-power regime, but a large facility is required.

This work introduces a novel way to overcome the low plasma current and technical complexity in beat-wave schemes. In our idea, two laser pulses counter-propagate (in contrast to conventional co-propagating schemes) and collide on a nano-dimensional overdense plasma sheet target. As the counter-propagating laser pulses interact with each other on a nano-thickness plasma, the restriction of low-density can be eliminated since the pulses need not propagate inside the plasma. Large plasma current becomes available as the charge carrier density is high in overdense plasmas. No complicated conversion mechanism of beat-to-THz is required; the beat-current can emit the THz wave directly into the vacuum through a thin (below the skin depth) nanoplasma sheet. No plasma shield of electromagnetic emission leads to high conversion efficiency. The number of oscillation cycles

[1]Department of Physics, Ulsan National Institute of Science and Technology, Ulsan 44919, Republic of Korea. [2]Department of Physics and Photon Science, Gwangju Institute of Science and Technology, Gwangju 61005, Republic of Korea. ✉email: mshur@unist.ac.kr

in THz pulses can be made arbitrarily large by increasing the duration of driving pulses. From these features, extremely intense multicycle THz pulses with a narrowband frequency spectrum at the beat-frequency of the laser pulses can be obtained with a high efficiency. Our two-dimensional (2D) and three-dimensional (3D) particle-in-cell (PIC) simulations show that such a THz source is capable of providing field strength of GV/m-level, and frequency tunability with a narrowband spectrum. Furthermore, our system preserves the advantage of a single-pulse-driven target, as the broadband THz radiation is emitted together with the desired narrowband one in a single setup.

Results

Beat-frequency THz and second-harmonic radiation generation.

For 2D PIC simulations, we used the well-known particle-in-cell code EPOCH[48] (see "Methods" section). The sketch of our scheme is shown in Fig. 1a. Two laser pulses with different frequencies, $\omega_1 = 2\pi c/\lambda_{L1}$ and $\omega_2 = 2\pi c/\lambda_{L2}$, where the wavelengths $\lambda_{L1} = 800$ nm and $\lambda_{L2} = 740$ nm, respectively, and c is the speed of light in vacuum, collide obliquely with each other at an angle $\theta_{col} = 35°$ on a plasma sheet target. The initial thickness and electron density of the plasma sheet are $d = 20$ nm and $n_{e0} = 5n_c$, respectively, where $n_c = m_e\varepsilon_0\omega_1^2/e^2$ is the critical density, ε_0 is the free space permittivity, m_e and $-e$ are the electron mass and charge. The laser pulses are s-polarized (to easily distinguish them from a p-polarized THz emission). The peak value of the normalized vector potential of the lasers is $a_{1,2} = eE_{1,2}/m_ec\omega_{1,2} = 0.6$ (corresponding to intensities $I_{L1} \simeq 7.7 \times 10^{17}$ W/cm² and $I_{L2} \simeq 9.5 \times 10^{17}$ W/cm²), and waist size $b_w = 5.8$ μm and pulse duration $\tau_L = 100$ fs (FWHM).

As both laser pulses interact with the plasma sheet, their beating exerts a ponderomotive force on the electrons of the plasma sheet that produces a nonlinear current, which emits the beat-frequency radiations ($\Delta\omega = \omega_1 - \omega_2$) in THz frequency range. Along with the THz radiation, the second-harmonics (SH) of the incident lasers are also generated due to the second-harmonic current that is produced by the second-harmonic component of ponderomotive force. The snapshots of the electric field E_z (it corresponds to the laser electric field for the s-polarized laser pulses), and the snapshots of the magnetic field B_z (it corresponds to the radiation field; the model indicates that it is always p-polarized to the laser incident plane, regardless of the laser polarization) are presented in Fig. 1b,c and 1d, respectively. The source of the emission is clearly at the colliding region of the laser pulses. The low-frequency part of this radiation could be isolated by applying a Gaussian-Filter to the total radiation field (filtered with $f \sim 60$ THz) as shown in Fig. 1e. As the beat ponderomotive force drives electron oscillations, the plasma electron density is strongly modulated in the colliding region, as shown in Fig. 1f–h. Here we note that when the emitted THz pulses propagate, strong diffraction appears (because the spot size of the colliding laser pulses is smaller than the THz wavelength). The diffraction can be reduced by increasing the laser spot size more than the THz wavelength.
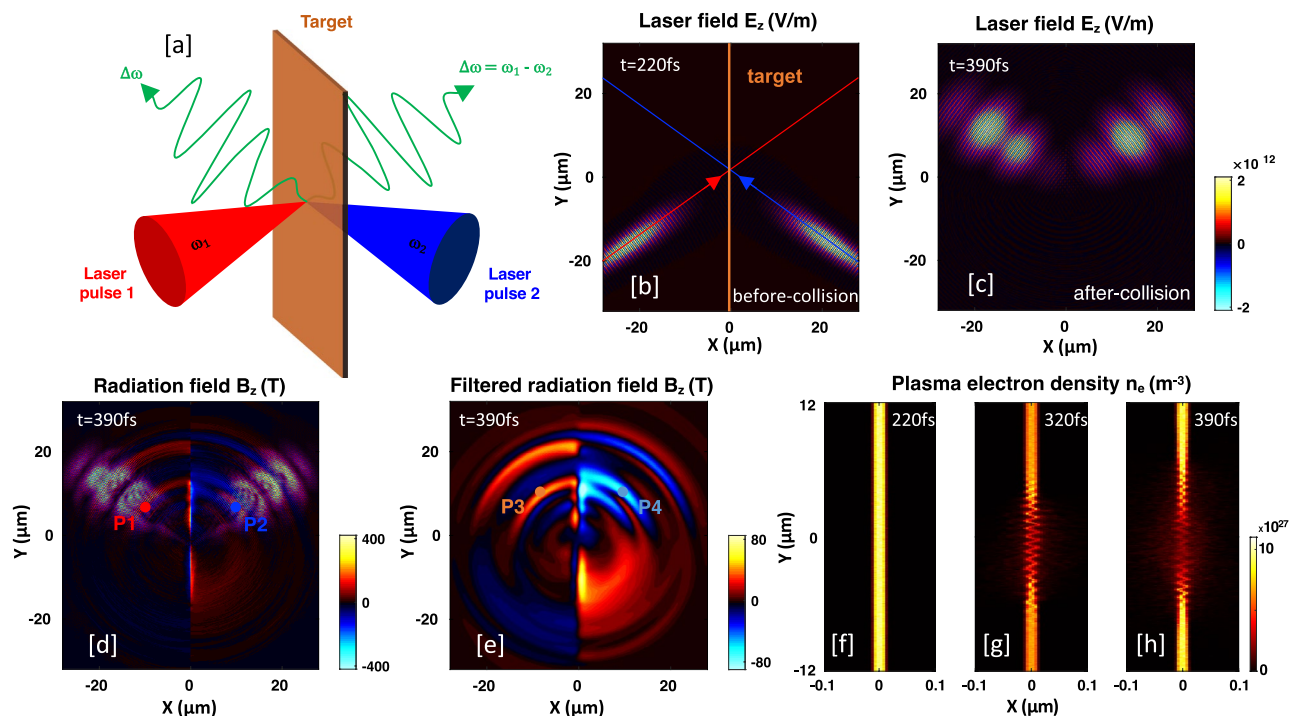

Figure 1. (a) Sketch of the scheme: Two laser pulses with different frequencies, ω_1 and ω_2 collide obliquely with each other on an overdense plasma sheet of nm thickness. From the region of the colliding laser pulses, beat-frequency radiation ($\Delta\omega = \omega_1 - \omega_2$) is emitted into the vacuum. Snapshots of spatial distributions of; (b,c) laser field E_z (V/m) (s-polarized), (d) total radiation field B_z (T) (p-polarized), (e) filtered radiation field B_z (T), and (f–h) plasma electron number density n_e (m⁻³), at different times; $t = 220$ fs, 320 fs, and 390 fs.

To determine the frequency of the emitted radiation in vacuum, we located virtual point probes at P1($x = -10$ μm, $y = 7$ μm), P2($x = 10$ μm, $y = 7$ μm), P3($x = -10$ μm, $y = 10$ μm), and P4($x = 10$ μm, $y = 10$ μm), to collect the electric and magnetic fields data. The probe positions are denoted by the filled circles in Fig. 1d,e. The temporal evolutions of the total and filtered radiation fields obtained from different probes are shown in Fig. 2a,b. The Fourier spectra of their temporal dependence have the dominant peaks at $2\omega_1$, $2\omega_2$ (SH of the laser pulses), $\omega_1 + \omega_2$, and a small peak at $\omega_1 - \omega_2$ (Fig. 2c). Here we note that the second harmonic is generated by reflection; $2\omega_1$ is dominant on the front (left) side of the target, while $2\omega_2$ on the rear (right) side of the target (indicated by the red and blue color lines, respectively). In this study, we focus only on the beat-frequency radiation, so we have removed the high-frequency components from the obtained spectra; Fig. 2d shows a dominant peak near the beat-frequency ($f_{\Delta\omega} \sim 30$ THz) (which represents the emission central frequency), and other smaller peaks at its harmonics $2(f_{\Delta\omega})$. They are obtained from the probe (P3) located on the front-side of the target. Also, the spectrum has a low-frequency peak near $f \sim 5$ THz, which we believe comes through the transition radiation by fast electrons generated from laser-target interactions via different mechanisms[49–51]. A strong direct-current (DC)-like, wideband (0 $\sim$ 10 THz) component is observed from the probe (P4) located on the rear-side of the target (Fig. 2d), which also comes through transition radiation, and comparable strength of the peak at beat-frequency is also found on the rear-side. So, the emitted radiation has a mixture of CTR and beat-frequency ponderomotive force-driven plasma currents. The peak field strengths reach up to 44.2T and 51.4T at ± 10 μm from the sheet surface, which is much higher than other THz sources reported so far.

Effects of duration and detuning of driving pulses. We now study the cases driven by much longer laser pulses, with duration $\tau_L = 500$ fs on the same target. Figure 3a shows the strong radiation on the front and back surfaces of the target. Interestingly, in the map of E_y (Fig. 3b), strong radiation is found at the top and bottom edges of the sheet, which could be related to antenna-like emission by shielding electron current flowing along the plasma sheet surface[52,53]. Figure 3c shows the temporal profiles of the magnetic field data collected by the point probes; P5($x = -10$ μm, $y = 10$ μm) and P6($x = 10$ μm, $y = 10$ μm), marked by filled orange and light-blue circles in Fig. 3a. Here it is noteworthy that the number of cycles in the radiation pulse has increased in accordance with the increase in pulse duration of the laser. The THz pulse duration is comparable to the laser pulse duration, indicating that THz radiation is generated all through pulse-plasma interaction. Compared to Fig. 2d, the bandwidth of the Fourier spectrum around the beat-frequency ($\sim$ 30 THz) and its second-harmonic ($\sim$ 60 THz) is considerably narrowed, up to 5.3% (Fig. 3d). The peak field strengths reach up to 29.5 T ($\simeq$ 8.85 GV/m) and 39.8 T ($\simeq$ 11.9 GV/m) on the front and rear sides of the target, respectively. Compara-
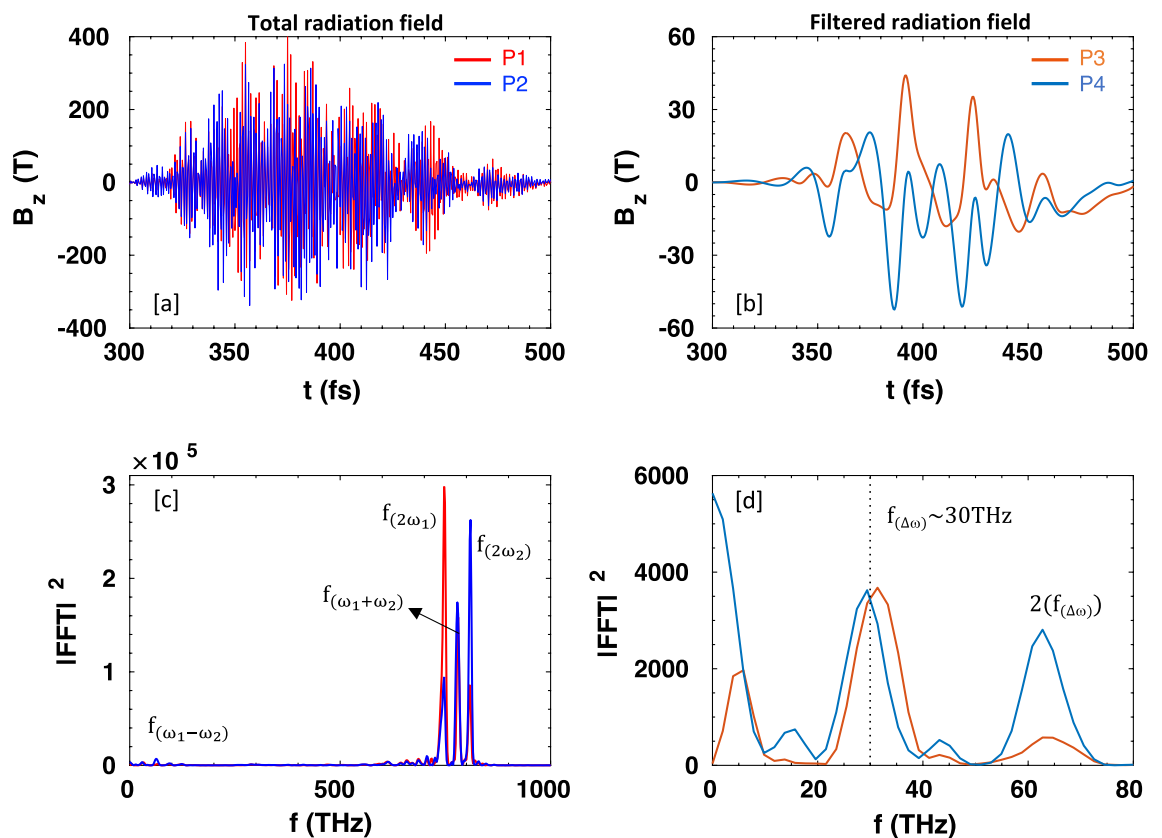

Figure 2. Temporal profiles of (**a**) total emitted radiation, (**b**) filtered beat-frequency radiation in vacuum, measured by the virtual point probes; P1, P2, P3, and P4, located 10 μm away from the emission spot, and (**c–d**) their corresponding power spectra.
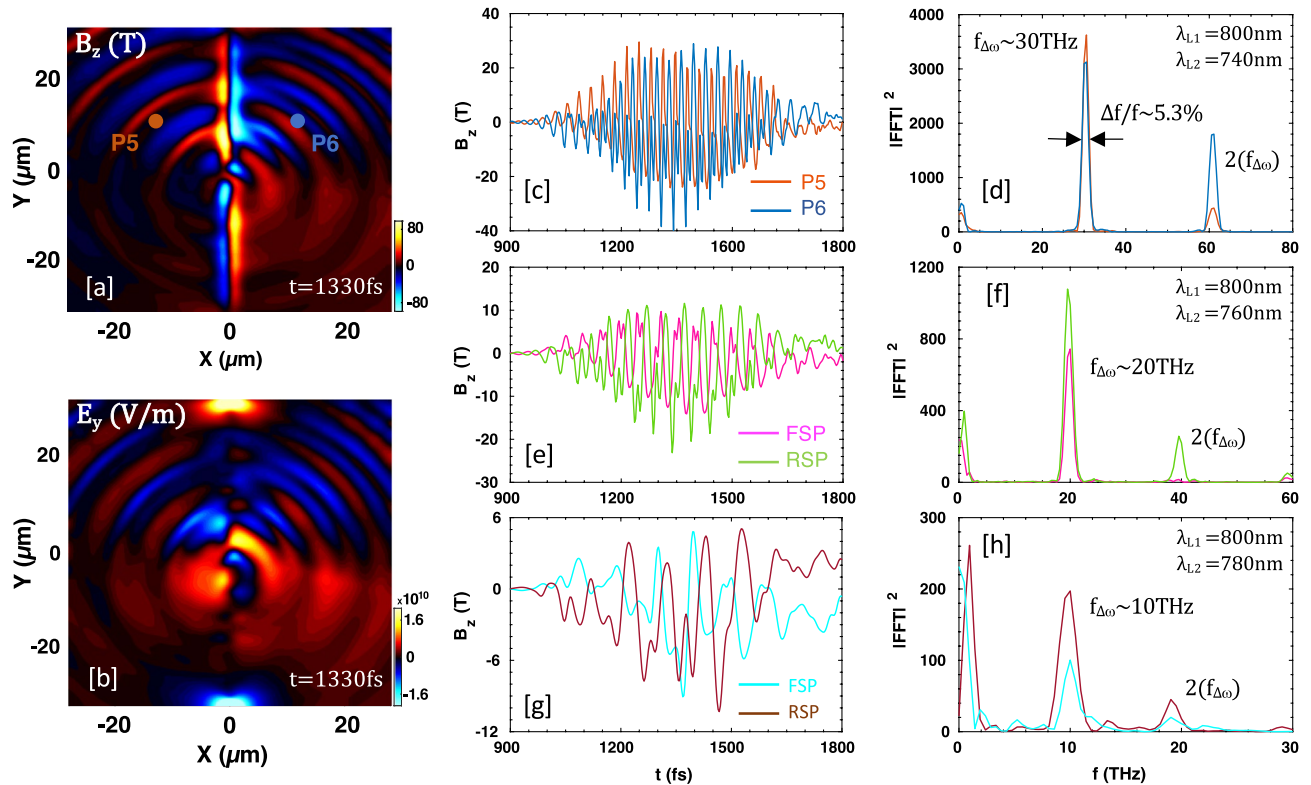
Figure 3. Snapshots of spatial distributions of (**a**) magnetic field B_z(T) and (**b**) electric field E_y(V/m) at $t = 1330$ fs for longer pulse duration $\tau_L = 500$ fs. The field data are filtered to extract the beat-frequency THz range. (**c**) Temporal evolutions of filtered magnetic fields which are acquired from virtual point probes; P5 and P6, and (**d**) their corresponding power spectra. When the wavelength of the second laser pulse is changed, temporal profiles and power spectra; (**e,f**) for $\lambda_{L2} = 760$ nm, and (**g,h**) for $\lambda_{L2} = 780$ nm.

ble strength of peak electric field of 10.8 GV/m was reported via conventional difference frequency mixing in AgGaS$_2$[54]. Here we notice that the second-harmonic of the beat-frequency on the right side is stronger than on the left side of the target. We have not yet identified the reason for that.

We also perform simulations to see the detuning effect of the driving pulses. Figure 3e represents the THz radiation field measured at the same probe positions as before [front-side probe (FSP) and rear-side probe (RSP)], when the wavelength of the second laser pulse is increased to $\lambda_{L2} = 760$ nm (corresponding to $\sim$ 20 THz). The radiation field amplitude decreases from the previous case with $\lambda_{L2} = 740$ nm, as the beat-current is proportional to the beat-frequency (actually the linear frequency dependence of radiation amplitude is common for the scheme that uses the plasma electrons as charge carriers). Its power spectrum has a main peak at the beat-frequency ($\sim$ 20 THz) (Fig. 3f). When the wavelength of the second laser pulse is increased even more up to 780 nm, the THz radiation again peaks at the beat-frequency, i.e. 10 THz (Fig. 3h). In the lower beat-frequency cases also, the THz pulse durations are comparable to the driving laser pulse duration (Fig. 3g), implying that by using longer laser pulses (e.g. $\sim$ 1 ps), the number of cycles in the radiation pulse and the beat-frequency peak value can be increased. Note that the low-frequency radiations near $f \sim$ 1 THz, throughout Fig. 3c–h, do not dramatically change as the second wavelength of the pulse increases, evidencing that the low-frequency radiation comes dominantly from single-laser-target interactions (i.e. CTR) rather than from the beating of lasers.

Effects of target parameters and collision angle of laser pulses. We now examine the effect of the plasma sheet thickness on beat-frequency THz radiation. Figure 4a shows the snapshot of the filtered radiation field for thickness $d = 200$ nm, with other parameters same as in Fig. 2. Differently from a thin target ($d = 20$ nm), the radiation fills the whole simulation domain (by contrast, upward radiation is dominant in Fig. 1e). Note that, it has different polarities at the front and back surfaces of the sheet. Radiation emission to the surface-normal direction is very small, i.e. conical emission in 3D space, typical of CTR. The temporal profiles of emitted radiation in vacuum and their spectra are illustrated in Fig. 4b. From a thick target ($d = 200$ nm), only the half-cycle, low-frequency radiation is generated; no beat-frequency radiation is observed. This is because the target is thicker than the skin depth, so the laser pulses cannot beat with each other. The target interacts with single pulses from either side and the radiation can be produced via CTR mechanism only.

Figure 4c shows the peak field strength of beat-frequency THz radiation decreases with increasing the thickness of the plasma sheet. We also performed the simulations preserving the surface density to 100 (nm$\times n_c$) for the sets; set-I, set-II, and set-III, and other parameters are the same as in Fig. 2. The temporal profiles of the filtered radiation field (measured at the front-side of the target only) are illustrated in Fig. 4d. We find that the
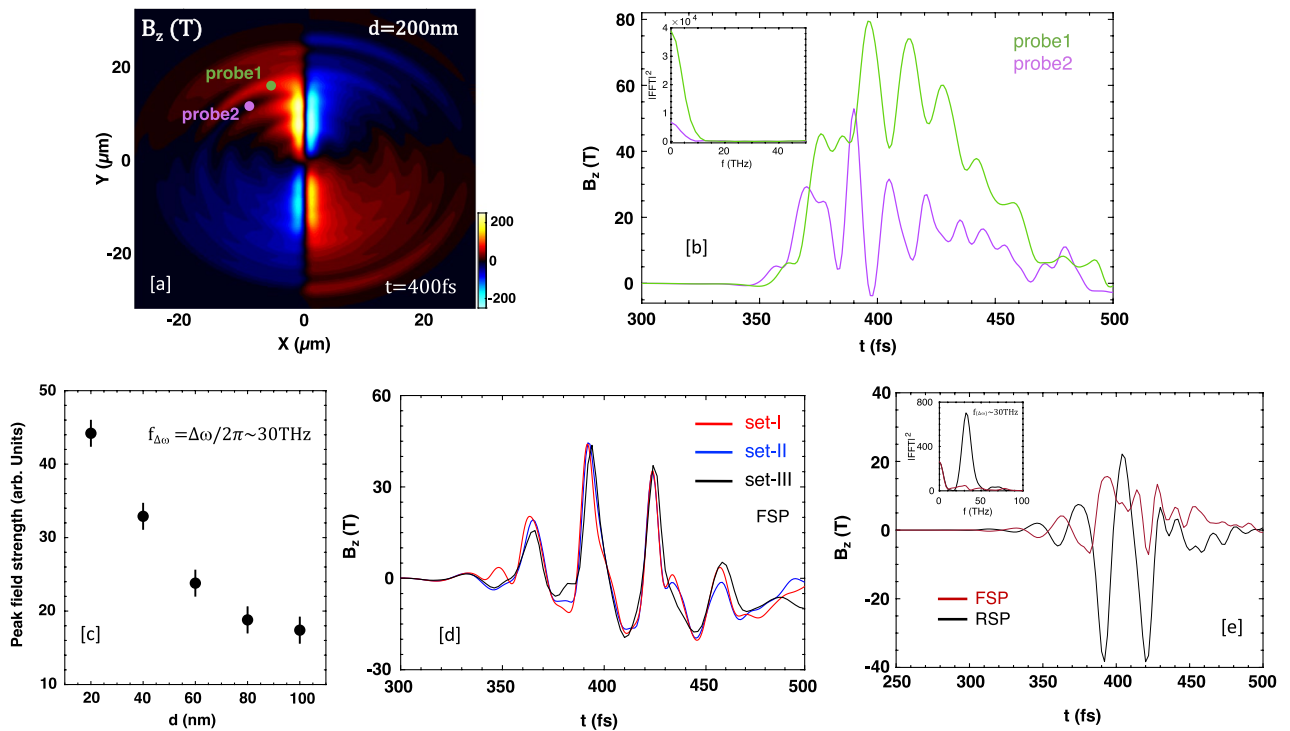
4

Figure 4. (**a**) Snapshot of spatial distribution of filtered magnetic field B_z(T) at $t = 400$ fs for target thickness $d = 200$ nm. (**b**) Temporal profiles of emitted radiation measured by; probe1($x = -5$ μm, $y = 15$ μm) and probe2 ($x = -10$ μm, $y = 10$ μm). (**c**) Peak field strength of beat-frequency radiation as a function of plasma sheet thickness. (**d**) Temporal profiles of emitted radiation measured by the front-side probe ($x = -10$ μm, $y = 10$ μm) for three different sets; set-I ($d = 20$ nm, $n_{e0} = 5n_c$), set-II ($d = 10$ nm, $n_{e0} = 10n_c$), and set-III ($d = 2$ nm, $n_{e0} = 50n_c$) from a preloaded plasma sheet target. (**e**) Temporal profiles of filtered radiation fields (measured by the front-side and rear-side probes located 10 μm away from the emission spot) from an unionized target, like a graphene sheet, and their corresponding power spectra.

beat-frequency emitted radiation changes only slightly for different thicknesses but with the same surface density. This result, along with the insensitivity to the density profile of the target, can be a great advantage in designing future experiments; one may use a free-diffused target starting from the ablation of high-density, but thin targets. In this case, THz emission may be insensitive to the delay between the ablating pulse and driver pulses. Another is the use of a graphene sheet target with thickness $\sim$ 2 nm and density $\sim$ 50 n_c, which is in the neutral state before being ionized. Furthermore, our 2D simulation results also suggest that this system can produce beat-frequency THz radiation with high-peak field strength on the rear-side of the sheet (Fig. 4e), but the front-side emission is significantly reduced compared to a pre-ionized plasma sheet target of the same thickness (see Fig. 4d: set-III). We have not yet figured out the reason for that.

Now we see the behavior of THz radiation yield for different colliding angles of the laser pulses. The average Poynting flux ($< S_{rad} > = (c/2\mu_0)|B_0|^2$, B_0 is the peak value of magnetic field B_z and μ_0 is the free space permeability) passing through the probing planes (actually probing lines in the 2D domain) at $x = \pm$ 10 μm (both left and right sides of the sheet) is integrated over y from $y_1 = -32$ μm, through $y_2 = +32$ μm, to obtain the power of THz emission. Figure 5a shows that the peak power of THz emission (filtered around $\sim f_{\Delta\omega}$) on both sides of the sheet, increases as the collision angle increases. Because the transverse current is increased for the larger colliding angles, resulting in an enhancement in the field strength of radiation pulses. Although the front-side emission power is lower than the rear-side one, it increases much faster with the collision angles compared to the rear-side emission. This is because the rear-side emission has stronger direct-current components than the front-side one when the colliding angle is small, however, the beat-frequency components are nearly equal on either side of the target and they also have the same emission rate, as shown in Fig. 5b (excluded low-frequency CTR from the emission). When the colliding angle is increased, the direct-current components on the rear-side get weaker, so the rate of emission is also reduced compared to the front-side one. For large collision angle $\theta_{col} > 50°$, the power of THz emission on both sides eventually saturates as the emission is confined near the sheet surfaces.

Theoretical analysis.

In our approach, THz radiation arises from the strong plasma current generated when two laser pulses collide with each other on a plasma sheet. During the interaction, both longitudinal and transverse currents are formed, carried by the plasma electrons. To calculate those currents, the electric field of the laser pulses can be described as follows:
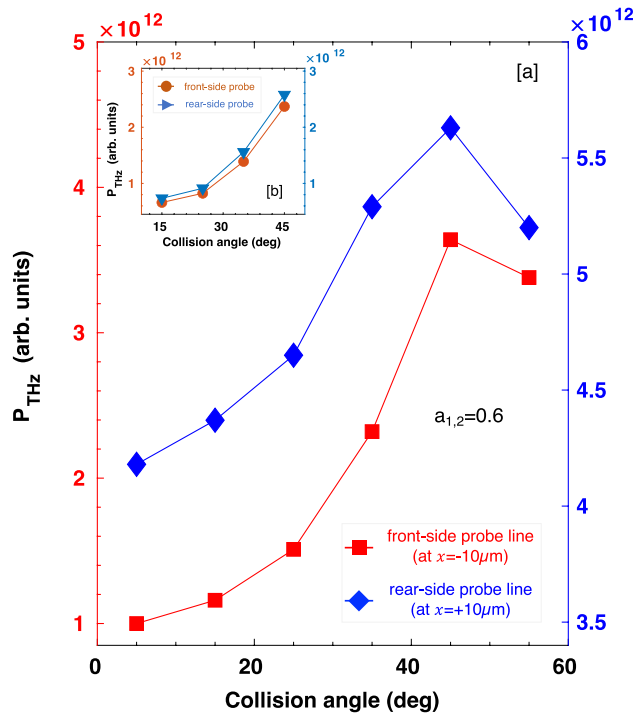
Figure 5. (**a**) Power of THz emission vs. colliding angles of the laser pulses. The power (including the contribution of non-beat-frequency components) is obtained by integrating THz intensity over y (from $-32\ \mu\text{m}$ through $+32\ \mu\text{m}$) passing through the probe lines at $x = \pm 10\ \mu\text{m}$. (**b**) Power of THz emission with beat-frequency components only.

$$\mathbf{E}_1 = \hat{z}\, A_1 e^{-i[\omega_1 t - (k_{1x} x + k_{1y} y)]}, \mathbf{E}_2 = \hat{z}\, A_2 e^{-i[\omega_2 t + (k_{2x} x - k_{2y} y)]}, \tag{1}$$

where $k_{1x} = (\omega_1/c)\cos\theta_{\text{col}}$, $k_{1y} = (\omega_1/c)\sin\theta_{\text{col}}$ and $k_{2x} = (\omega_2/c)\cos\theta_{\text{col}}$, $k_{2y} = (\omega_2/c)\sin\theta_{\text{col}}$ are the wave-numbers of the first and second laser pulses and θ_{col} is their collision angle. The beat-frequency ($\Delta\omega = \omega_1 - \omega_2$) ponderomotive force (PF) on plasma electrons is given by:

$$\mathbf{F}_{\text{P}(\Delta\omega)} = -\frac{e^2(\mathbf{k}_1 - \mathbf{k}_2)}{2mi\omega_1\omega_2}\mathbf{E}_1.\mathbf{E}_2^*, \tag{2}$$

where m and $-e$ are the electron mass and charge. The current density is given by, $\mathbf{J}_{(\Delta\omega)} = -en_0\mathbf{v}_{(\Delta\omega)}$, (where n_0 is the plasma electron density and $\mathbf{v}_{(\Delta\omega)}$ is the plasma electron velocity due to PF), which lies in the $x - y$ plane, so it has two components:

$$J_x = \text{j}_\text{s}\left(\frac{\omega_1 + \omega_2}{\Delta\omega}\right)\cos\theta_{\text{col}}e^{-i\left[(\Delta\omega)t - ((k_{1x}+k_{2x})x + (k_{1y}-k_{2y})y)\right]}, \tag{3}$$

$$J_y = \text{j}_\text{s}\left(\frac{\omega_1 - \omega_2}{\Delta\omega}\right)\sin\theta_{\text{col}}e^{-i\left[(\Delta\omega)t - ((k_{1x}+k_{2x})x + (k_{1y}-k_{2y})y)\right]}, \tag{4}$$

where $\text{j}_\text{s} = a_1 a_2^* m\varepsilon_0 c^2\omega_p^2/2e$, $\omega_p^2 = n_0 e^2/m\varepsilon_0$, is the plasma frequency, ε_0 is the free space permittivity, $a_1 = eA_1/m\omega_1 c$ and $a_2^* = eA_2^*/m\omega_2 c$ are the normalized amplitude of the lasers.

To estimate the radiated power, we assumed the target thickness is much smaller than the THz wavelength. Therefore, in this limit, the nonlinear current source can be treated like a wire antenna as far as the radiation field is concerned[55]. The total radiated THz power can be described by; $\text{P}_{\text{THz}} = \int_0^{2\pi}\int_0^{\pi}\mathbf{S}_{\text{avg}}r^2\sin\theta d\theta d\Phi$, where $\mathbf{S}_{\text{avg}} = \hat{r}|B|^2 c/2\mu_0$ is the time average Poynting's vector, μ_0 is the free space permeability, and magnetic field of beat wave is $\mathbf{B} = \nabla \times \mathbf{A} \simeq i(\Delta\omega/c)\hat{r}\times\mathbf{A}$, where $\mathbf{A}$ is the vector potential at the far point. Thus,

$$\text{P}_{\text{THz}} = \frac{\pi c m^2\omega_p^4\sin^2\theta_{\text{col}}}{2\mu_0 e^2}\left(\frac{a_1 a_2^*}{2}\right)^2\int_0^{\pi}\frac{\sin^2\left[\Delta\omega L(1-\cos\theta)/2c\right]\sin^3\theta I_0^2}{(1-\cos\theta)^2}d\theta, \tag{5}$$

where $I_0 = \int_0^{r_d} J_0(\Delta\omega\rho_i\sin\theta/c)\rho_i d\rho_i$, $J_0(x)$ is the Bessel function of first kind zero order, L and r_d are the length and radius of the wire. In the calculation, we have considered the radiation driven by the beat-frequency pon-deromotive force only. The above equation predicts that the emission power increases with $\sin^2\theta_{\text{col}}$ for $\theta_{\text{col}} < 90°$. There is no THz emission for normal incidence $\theta_{\text{col}} = 0°$ because there is no transverse current component.

Figure [6]a shows the lasers-to-THz power conversion efficiency as a function of the normalized vector potential of lasers, and a comparison of the theoretically obtained efficiency (from Eq. ([5])) with simulation results. The efficiency increases with $a_{1,2}$, reaching around 0.02% when the laser intensities are close to 10^{18} W/cm^2. Note that, if the intensity $> 10^{18}$ W/cm^2, it begins to saturate presumably due to relativistic effects. Here it can be seen that the simulated efficiency (solid-red-circle) is higher than the theoretical efficiency due to the non-beat-frequency components. When only the beat-frequency components are taken into account in the calculation of the efficiency, the efficiency (solid-green-circle) decreases and approaches the theoretical result. The theoretical scaling is proportional to the square of the normalized vector potential of lasers. Figure [6]b shows that the efficiency increases with increasing the beating frequency.

Three-dimensional PIC simulations

In the previous section, we have dealt only with 2D PIC simulations for the foundation of a novel method supported by theoretical analysis. The realistic model of the proposed system that can be applied to the experiment needs to develop through a three-dimensional simulation study. Therefore, we also performed 3D simulations for a similar situation using EPOCH code. For that we have chosen a target of 56 μm wide, 48 μm tall, 100 nm thick, and has the electron density of $1.0 n_c$ (to preserve the surface density to $100 (\text{nm} \times n_c)$ same as in our 2D simulations). The target is tilted at an angle of 45° with respect to both laser propagation directions. The laser pulses are s-polarized with intensities; $I_{L1} \simeq 7.7 \times 10^{17}$ W/cm^2 and $I_{L2} \simeq 9.5 \times 10^{17}$ W/cm^2 (same as in 2D simulation), with 8.4 μm spot diameter, but use only a 30 fs (FWHM) pulse duration due to limitation by computational resources. The simulation domain is 60 μm (in x-direction and y-direction), and 50 μm(in z-direction), with the grid sizes $dx = dy = dz = \lambda_{L1}/12.5$, and filled with 10 numerical macro-particles per cell. Figure [7]a displays an isosurface of filtered beat-frequency THz radiation field (in red-color) at $t = 240$ fs. The snapshots of the 2D slices (cut through x-, y-, and z-axis) of the THz radiation field show that the emission originates from the colliding region of laser pulses (Fig. [7]b–d). As time goes on, the radiation fills the entire simulation domain, but strong emission is found in the upward region and weak emission in the downward region of the sheet. The emitted THz pulses have one oscillation cycle because their duration is comparable to the laser pulse duration (~ 30 fs). The peak field strength reaches more than 10 GV/m in the 3D simulation, but it is lower than the 2D simulation result for the same parameters (Fig. [7]e). However, the X–Y spatial distribution of the THz field (Fig. [7]f) is similar to the 3D simulation result. This strongly indicates that the beat-frequency mechanism will work efficiently for the experiment.

Conclusion

We proposed a novel scheme to obtain narrowband, readily tunable, compact, and experiment-friendly THz sources based on the oblique collision of two-detuned laser pulses on a nano-dimensional overdense plasma sheet target. The process of THz emission and resulting THz characteristics were investigated by using two- and three-dimensional particle-in-cell simulations. In contrast to single-pulse-driven targets, where long half-cycle THz pulses are generated with a broadband spectrum via CTR mechanism, by irradiating the rear surface of the target with another laser pulse, we produced multicycle, narrowband THz radiation at the beating frequency, dominating over the CTR. The THz radiation was generated due to the ponderomotive force-driven plasma current in
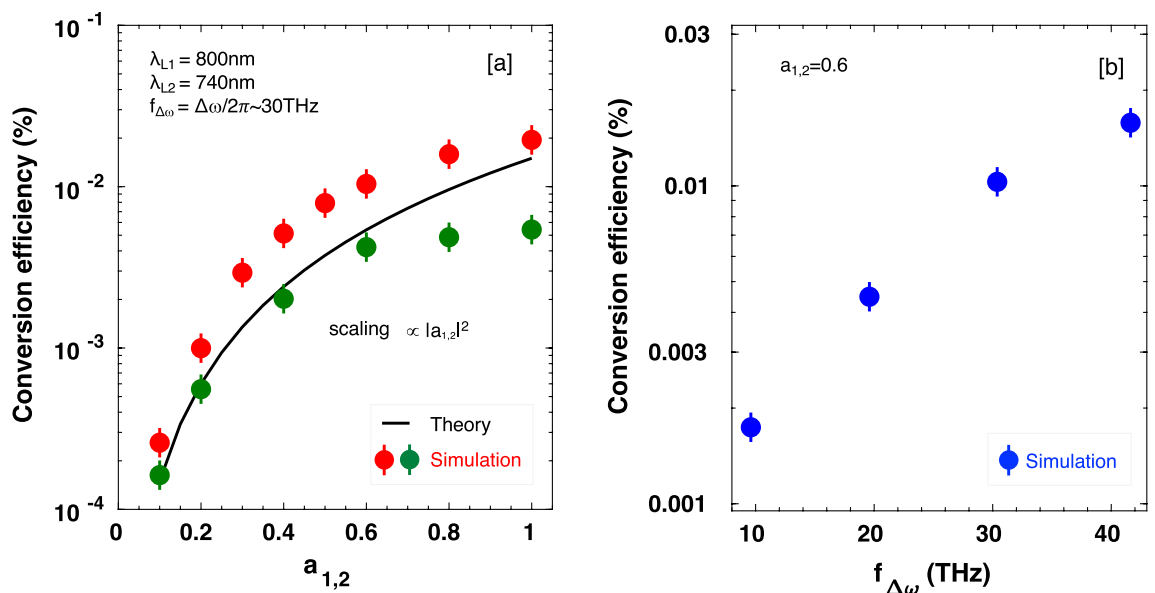

Figure 6. Efficiency of power conversion from lasers-to-THz emissions as a function of; (**a**) normalized vector potential of lasers $a_{1,2}$, (**b**) central-frequency of THz radiation $f_{\Delta\omega}$. The solid-red, -green, and -blue circles are from simulation results (measured at ± 10 μm from the emission spot), and the solid black line is from theoretical results.
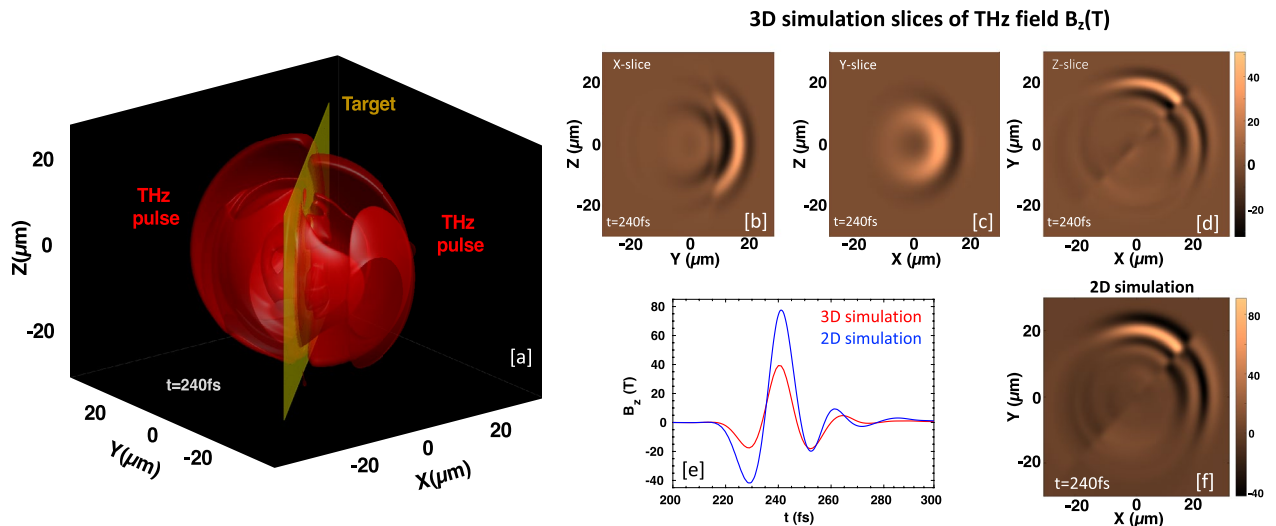
3D simulation slices of THz field B$_z$(T)

Figure 7. (**a**) 3D isosurface of beat-frequency THz radiation field (in red-color) at $t = 240$ fs. (**b**–**d**) 2-D slices (cut through x-, y-, and z-axis) of the THz radiation field. (**e**) Comparison of THz field strength (measured on the front-side of the target) through 2D and 3D PIC simulations for the same set of parameters. (**f**) Snapshot of X–Y spatial distribution of THz radiation field from 2D simulation.

the colliding region. We obtained extremely intense THz radiation of 40 TW/cm^2, with peak fields up to ~ 11.9 GV/m and 39.8 T at 10 μm from the emissionspot, with central frequency $f \sim 30$ THz and spectral bandwidth $\Delta f/f \simeq 5.3\%$ for $\tau_L = 500$ fs. The number of cycles of THz oscillation can be increased arbitrarily by increasing the driving pulse duration, which can provide a very narrowband spectrum. By using much longer laser pulses (~ 1 ps), the spectral bandwidth can be increased up to 3.28%. For the laser intensities $> 10^{18}$ W/cm^2, the emitted THz pulse energy was about 0.1 mJ. Such an extremely intense narrowband THz source will be suitable for various ambitious applications such as compact electron accelerators[44] and pump-probe experiments[45–47]. We believe our results will greatly help in designing future experiments on the proposed system.

Methods

Simulations code and parameters. The 2D and 3D simulations were performed using fully relativistic particle-in-cell code, EPOCH (Extendable PIC Open Collaboration)[48]. Maxwell's equations are solved in this code using the finite-difference time-domain (FDTD) method in 2D3V (two-dimensional configuration space and three-dimensional momentum space) geometry. The electric and magnetic fields are specified on Yee staggered grids[56], and the Boris algorithm[57] is used for solving the equation of motion of the particles. The currents required for the Maxwell solver are calculated from the particle motion using Esirkepov's method[58] which is a generalization of the Villasenor and Buneman current deposition scheme[59].

In our simulations, both laser pulses are injected into the simulation domain from the left and right boundaries, colliding on the plasma sheet target with different thicknesses and densities. The two-dimensional simulation domain is 56 μm long and 64 μm wide with a grid size $dx = dy = \lambda_{L1}/160$ in the x- and y-directions, respectively. Each grid cell is filled with 40 numerical macro-particles (a total of over 10^6 particles in the entire simulation domain). The time step is set to ensure Courant conditions: $\Delta t = 0.99\Delta x/(c\sqrt{2}) \simeq 1.667 \times 10^{-17}$. For both particles and fields, we use the *simple_laser* boundary condition at the left and right box boundaries ($x = \mp 28$ μm) and the *simple_outflow* boundary condition at the top and bottom box boundaries ($y = \pm 32$ μm). We used the BSI (barrier-suppression ionization) model in EPOCH code for the simulation including field ionization.

Data availability

The data supporting this study's findings are available from the corresponding author upon reasonable request.

References

1. Tonouchi, M. Cutting-edge terahertz technology. *Nat. Photonics* **1**, 97–105 (2007).
2. Zhang, X. C., Shkurinov, A. & Zhang, Y. Extreme terahertz science. *Nat. Photonics* **11**, 16–18 (2017).
3. Pickwell, E. & Wallace, V. Biomedical applications of terahertz technology. *J. Phys. D Appl. Phys.* **39**, R301–R310 (2006).
4. Mittleman, D. M. Twenty years of terahertz imaging. *Opt. Express* **26**, 9417–9431 (2018).
5. Jepsen, P. U., Cooke, D. G. & Koch, M. Terahertz spectroscopy and imaging—Modern techniques and applications. *Laser Photon. Rev.* **5**, 124–166 (2011).
6. Baxter, J. B. & Guglietta, G. W. Terahertz spectroscopy. *Anal. Chem.* **83**, 4342–4368 (2011).
7. Liu, J., Dai, J., Chin, S. L. & Zhang, X. C. Broadband terahertz wave remote sensing using coherent manipulation of fluorescence from asymmetrically ionized gases. *Nat. Photonics* **4**, 627–631 (2010).
8. Koenig, S. *et al.* Wireless sub-THz communication system with high data rate. *Nat. Photonics* **7**, 977–981 (2013).

9. Kemp, M. Explosives detection by terahertz spectroscopy—A bridge too far. *IEEE Trans. THz Sci. Technol.* **1**, 282–292 (2011).
10. Auston, D. H., Cheung, K., Valdmanis, J. & Kleinman, D. Cherenkov radiation from femtosecond optical pulses in electro-optic media. *Phys. Rev. Lett.* **53**, 1555–1558 (1984).
11. Stepanov, G. A., Bonacina, L., Chekalin, S. V. & Wolf, J. P. Generation of $30\mu J$ single-cycle terahertz pulses at 100 Hz repetition rate by optical rectification. *Opt. Lett.* **33**, 2497–2499 (2008).
12. Fulop, J. A. *et al.* Efficient generation of THz pulses with 0.4 mJ energy. *Opt. Express* **22**, 20155–20163 (2014).
13. Huang, W. R. *et al.* Highly efficient terahertz pulse generation by optical rectification in stoichiometric and cryo-cooled congruent lithium niobate. *J. Mod. Opt.* **62**, 1486–1493 (2015).
14. Vicario, C. *et al.* Generation of 0.9 mJ THz pulses in DSTMS pumped by a $Cr : Mg_2SiO_4$ laser. *Opt. Lett.* **39**, 6632–6635 (2014).
15. Vicario, C., Monoszlai, B. & Hauri, C. P. GV/m single-cycle terahertz fields from a laser-driven large-size partitioned organic crystal. *Phys. Rev. Lett.* **112**, 213901–5 (2014).
16. Hamster, H., Sullivan, A., Gordon, S., White, W. & Falcone, R. W. Subpicosecond, electromagnetic pulses from intense laser-plasma interaction. *Phys. Rev. Lett.* **71**, 2725–2728 (1993).
17. Sheng, Z. M., Mima, K., Zhang, J. & Sanuki, H. Emission of electromagnetic pulses from laser wakefields through linear mode conversion. *Phys. Rev. Lett.* **94**, 95003–5 (2005).
18. Kumar, M., Lee, K., Park, S. H., Jeong, Y. U. & Vinokurov, N. Terahertz radiation generation by nonlinear mixing of two lasers in a plasma with density hill. *Phys. Plasmas* **24**, 033104–5 (2017).
19. Kwon, K. B. *et al.* High-energy, Short-duration bursts of coherent terahertz radiation from an embedded plasma dipole. *Sci. Rep.* **8**, 145–9 (2018).
20. Kumar, M., Kang, T., Kylychbekov, S., Song, H. S. & Hur, M. S. Simulation study of phase-matched THz emission from an axially modulated magnetized plasma. *Phys. Plasmas* **28**, 033101–11 (2021).
21. Amico, C. D. *et al.* Conical forward THz emission from femtosecond-laser-beam filamentation in air. *Phys. Rev. Lett.* **98**, 235002–4 (2007).
22. Kim, K. Y., Glownia, J. H., Taylor, A. J. & Rodriguez, G. Terahertz emission from ultrafast ionizing air in symmetry-broken laser fields. *Opt. Express* **15**, 4577–4584 (2007).
23. Dai, J., Xie, X. & Zhang, X. C. Detection of broadband terahertz waves with a laser-induced plasma in gases. *Phys. Rev. Lett.* **97**, 103903–4 (2006).
24. Liu, K., Koulouklidis, A. D., Papazoglou, D. G., Tzortzakis, S. & Zhang, X. C. Enhanced terahertz wave emission from air-plasma tailored by abruptly autofocusing laser beams. *Optica* **3**, 605–608 (2016).
25. Kuk, D. *et al.* Generation of scalable terahertz radiation from cylindrically focused two-color laser pulses in air. *Appl. Phys. Lett.* **108**, 121106–5 (2016).
26. Leemans, W. P. *et al.* Observation of terahertz emission from a laser-plasma accelerated electron bunch crossing a plasma-vacuum boundary. *Phys. Rev. Lett.* **91**, 074802–4 (2003).
27. Schroeder, C. B., Esarey, E., Tilborg, J. V. & Leemans, W. P. Theory of coherent transition radiation generated at a plasma-vacuum interface. *Phys. Rev. E* **69**, 016501–12 (2004).
28. Liao, G. Q. *et al.* Demonstration of coherent terahertz transition radiation from relativistic laser-solid interactions. *Phys. Rev. Lett.* **116**, 205003–6 (2016).
29. Liao, G. Q. *et al.* Intense terahertz radiation from relativistic laser-plasma interactions. *Plasma Phys. Control. Fusion* **59**, 014039–014046 (2017).
30. Dechard, J., Davoine, X. & Berge, L. THz generation from relativistic plasmas driven by near- to far-infrared laser pulses. *Phys. Rev. Lett.* **123**, 264801–6 (2019).
31. Ding, W. J., Sheng, Z. M. & Koh, W. S. High-field half-cycle terahertz radiation from relativistic laser interaction with thin solid targets. *Appl. Phys. Lett.* **103**, 204107–204115 (2013).
32. Gopal, A. *et al.* Observation of gigawatt-class THz pulses from a compact laser-driven particle accelerator. *Phys. Rev. Lett.* **111**, 074802–5 (2013).
33. Gopal, A. *et al.* Observation of energetic terahertz pulses from relativistic solid density plasmas. *New J. Phys.* **14**, 083012–083023 (2012).
34. Li, Y. T. *et al.* Strong terahertz radiation from relativistic laser interaction with solid density plasmas. *Appl. Phys. Lett.* **100**, 254101–4 (2012).
35. Li, C. *et al.* Effects of laser-plasma interactions on terahertz radiation from solid targets irradiated by ultrashort intense laser pulses. *Phys. Rev. E* **84**, 036405–6 (2011).
36. Jin, Z. *et al.* Highly efficient terahertz radiation from a thin foil irradiated by a high-contrast laser pulse. *Phys. Rev. E* **94**, 033206–5 (2016).
37. Herzer, S. *et al.* An investigation on THz yield from laser-produced solid density plasmas at relativistic laser intensities. *New J. Phys.* **20**, 063019–063034 (2018).
38. Liao, G. Q. *et al.* Towards terawatt-scale spectrally tunable terahertz pulses via relativistic laser-foil interactions. *Phys. Rev. X* **10**, 031062–11 (2020).
39. Liao, G. Q. *et al.* Multi-millijoule coherent terahertz bursts from picosecond laser-irradiated metal foils. *Proc. Natl. Acad. Sci.* **116**, 3994–3999 (2019).
40. Mondal, S. *et al.* Aligned copper nanorod arrays for highly efficient generation of intense ultra-broadband THz pulses. *Sci. Rep.* **7**, 40058–40066 (2017).
41. Tokita, S., Sakabe, S., Nagashima, T., Hashida, M. & Inoue, S. Strong sub-terahertz surface waves generated on a metal wire by high-intensity laser pulses. *Sci. Rep.* **5**, 8268–8274 (2015).
42. Zhang, J., Ban, X., Wan, F. & Lv, C. Terahertz emission enhanced by a laser irradiating on a T-type target. *Appl. Sci.* **12**, 4464–4476 (2022).
43. Spies, J. A. *et al.* Terahertz spectroscopy of emerging materials. *J. Phys. Chem. C* **124**, 22335–22346 (2020).
44. Nanni, E. A. *et al.* Terahertz-driven linear electron acceleration. *Nat. Commun.* **6**, 8486–8494 (2015).
45. Forst, M. *et al.* Nonlinear phononics as an ultrafast route to lattice control. *Nat. Phys.* **7**, 854–856 (2011).
46. Dienst, A. *et al.* Bi-directional ultrafast electric-field gating of interlayer charge transport in a cuprate superconductor. *Nat. Photonics* **5**, 485–488 (2011).
47. Bakker, D. J., Peters, A., Yatsyna, V., Zhaunerchyk, V. & Rijs, A. M. Far-infrared signatures of hydrogen bonding in phenol derivatives. *J. Phys. Chem. Lett.* **7**, 1238–1243 (2016).
48. Arber, T. D. *et al.* Contemporary particle-in-cell approach to laser-plasma modelling. *Plasma Phys. Control. Fusion* **57**, 113001–113027 (2015).
49. Brunel, F. Not-so-resonant, resonant absorption. *Phys. Rev. Lett.* **59**, 52–57 (1987).
50. Xu, H., Sheng, Z. M., Zhang, J. & Yu, M. Y. Intensity-dependent resonance absorption in relativistic laser-plasma interaction. *Phys. Plasmas* **13**, 123301–7 (2006).
51. Bauer, D. & Mulser, P. Vacuum heating versus skin layer absorption of intense femtosecond laser pulses. *Phys. Plasmas* **14**, 023301–11 (2007).
52. Zhuo, H. B. *et al.* Terahertz generation from laser-driven ultrafast current propagation along a wire target. *Phys. Rev. E* **95**, 013201–5 (2017).

53. Dechard, J., Davoine, X., Gremillet, L. & Berge, L. Terahertz emission from submicron solid targets irradiated by ultraintense femtosecond laser pulses. *Phys. Plasmas* **27**, 093105–9 (2020).
54. Sell, A., Leitenstorfer, A. & Huber, R. Phase-locked generation and field-resolved detection of widely tunable terahertz pulses with amplitudes exceeding 100 MV/cm. *Opt. Lett.* **33**, 2767–2769 (2008).
55. Kumar, M. & Tripathi, V. K. Terahertz generation by nonlinear mixing of laser pulses in a clustered gas. *Phys. Plasmas* **18**, 053105–5 (2011).
56. Yee, K. S. Numerical solution of initial boundary value problems involving Maxwell's equations in isotropic media. *IEEE Trans. Antennas Propag.* **14**, 302–307 (1966).
57. Boris, J. P. *Proceedings of 4th Conference on the Numerical Simulation of Plasmas* 3–67 (NRL, 1970).
58. Esirkepov, T. Exact charge conservation scheme for particle-in-cell simulation with an arbitrary form-factor. *Comp. Phys. Commun.* **135**, 144–153 (2001).
59. Villasenor, J. & Buneman, O. Rigorous charge conservation for local electromagnetic field solvers. *Comp. Phys. Commun.* **69**, 306–316 (1992).

Acknowledgements

Author contributions

M.K., M.S.H., and H.S. conceived the fundamental idea. M.K. performed the 2D/3D PIC simulations, and analysis of the simulation results. Theoretical analysis was done by H.S.S., J.L., and D.P. The manuscript was written by M.K. and M.S.H., with contributions from all authors.

Competing interests

The authors declare no competing interests.

Additional information

Correspondence and requests for materials should be addressed to M.S.H.

Reprints and permissions information is available at www.nature.com/reprints.

Publisher's note Springer Nature remains neutral with regard to jurisdictional claims in published maps and institutional affiliations.